Int. J. Electrochem. Sci., 7 **(2012)** 1288 - 1302

International Journal of
ELECTROCHEMICAL
SCIENCE
www.electrochemsci.org

Mechanical Properties and Corrosion Behaviour of Nanostructured Cu-rich CuNi Electrodeposited Films

Aïda Varea[1,*], *Eva Pellicer*[1], *Salvador Pané*[2], *Bradley J. Nelson*[2], *Santiago Suriñach*[3],
Maria Dolors Baró[3] *and Jordi Sort*[3]

[1] Departament de Física, Facultat de Ciències, Universitat Autònoma de Barcelona, E-08193 Bellaterra, Spain.
[2] Institute of Robotics and Intelligent Systems (IRIS), ETH Zurich, CH-8092 Zurich, Switzerland.
[3] Institució Catalana de Recerca i Estudis Avançats (ICREA) and Departament de Física, Universitat Autònoma de Barcelona, E-08193 Bellaterra, Spain.
[*]E-mail: aida.varea.espelt@gmail.com

Received: 28 November 2011 / *Accepted:* 4 January 2012 / *Published:* 1 February 2012

Nanocrystalline Cu-rich CuNi alloy thin films (with copper content ranging from 22 to 97 at%) have been grown by electrodeposition, using galvanostatic conditions in an electrolytic bath containing Ni and Cu sulphates with a [Ni(II)]/[Cu(II)] molar ratio of 11. The Cu content is tuned by varying the applied current density during deposition. The nanoscrystalline nature of Cu-rich CuNi thin films has been achieved using saccharine as a grain refinement agent, although for high Cu content (> 90 at%) the refinement effect is less pronounced. Due to the nanocrystalline character of the films, low surface roughness, good compactness, and outstanding mechanical properties (e.g. nanoindentation hardness values of approximately 7 GPa) are obtained, particularly for Cu percentages below 70 at%. The presence of stacking faults also contributes to the observed high strength. The films show good corrosion protective behaviour in a 3.5 wt% NaCl medium, with corrosion potentials more positive than the bare substrate (pure-Cu) and lower corrosion current density values ranging from 1.8 to 5.4 μA/cm^2.

Keywords:

1. INTRODUCTION

Owing to their outstanding properties, pure copper and copper-rich alloys are being extensively used in a wide range of technological and metallurgical applications. For example, the combination of high electrical and thermal conductivities has prompted the utilization of these materials in microelectronic devices and integrated circuits [1]. In addition, Cu is mechanically softer and shows better ductility than many other metals, which is advantageous in terms of mechanical workability and permits the manufacture of microwires and a variety of devices with small lateral sizes. However, a large hardness may be desirable in certain applications, for example when Cu has to be subject to high tension in a welding. In principle, one can increase Cu strength by reducing the grain size (i.e., work hardening) or by alloying it with another metal. Depending on the alloying element, there are basically two mechanisms that cause mechanical hardening: (i) solid solution strengthening (Cu-Zn, Cu-Mn, Cu-Ni or Cu-Si) [1,2], and (ii) precipitation hardening (Cu-Be, Cu-Cr or Cu-Zr) [2].

The binary Cu-Ni system constitutes one of the most appealing Cu-based alloys due to its superior and tuneable mechanical properties as well as outstanding corrosion resistance. In particular, Cu-rich CuNi alloys have been used for many years in seawater, where they offer high resistance against bio-fouling [3]. Some CuNi alloys also serve as heat exchanger tube materials in coolant systems in nuclear power plants [4]. Additionally, Ni-rich CuNi deposits (i.e., for Ni content larger than 70 at%) are known to be ferromagnetic [5].

With the advent of nanotechnology new applications are being developed which often require novel or improved properties that only nanostructured or nanocrystalline materials can provide [6-8]. Nanostructured CuNi alloys can be fabricated by different methods such as sputtering, severe plastic deformation or electrodeposition (ED). ED offers several advantages as compared to other deposition techniques. It consists of a rather simple and cost-effective setup that can work without the need of high vacuum or high temperature conditions, samples can be grown at high deposition rates, there are no limitations on substrate geometry, and films several hundreds of microns thick can be easily prepared [9]. In addition, ED also allows precise tailoring of the alloy composition (and, consequently, of the resulting mechanical, magnetic and corrosion properties), simply by varying the working potential or the applied current density during film growth. Moreover, the deposition can be performed on a wide variety of substrate shapes, including pre-patterned substrates, thus rendering ED an adequate technique to fabricate micro-/nano-electromechanical systems (MEMS/NEMS) with complex geometries.

In previous works we have reported the mechanical properties, corrosion resistance and thermal stability of nanocrystalline electrodeposited Ni-rich Cu_xNi_{1-x} alloys ($0.13 \leq x \leq 0.55$) [5,10,11]. In this article, instead, we explore the Cu-rich region of the phase diagram ($0.22 \leq x \leq 0.97$). One of the drawbacks usually encountered in the ED of CuNi alloys with high Cu content is that Cu tends to exhibit a dendritic growth making it difficult to obtain flat surfaces. Nevertheless, the dendritic growth can be avoided to a certain extent with a suitable bath formulation [12-14]. The resulting films with flat surfaces, which would be appropriate for their implementation in MEMS/NEMS, show good wear resistance and excellent anti-corrosion properties.

2. EXPERIMENTAL

2.1. Instrumentation

A three-electrode cell connected to a PGSTAT120 Autolab potenciostat/galvanostat (Ecochemie) has been used. A double junction Ag|AgCl (E = +0.210V/SHE) acted as reference electrode (RE) (Metrohm AG) with 3M KCl as the inner solution and 1M Na_2SO_4 as the outer solution. A Pt sheet served as counter electrode (CE). A vitreous carbon cylindrical rod with $\pi \cdot 10^{-2}$ cm^2 surface area was used as working electrode (WE) for cyclic voltammetry (CV) studies, whereas silicon (100) substrates, with e-beam evaporated Ti (25 nm)/Cu (250 nm) adhesion/seed layers served as the WE for deposit growth. The working area ranged between (0.25 ± 0.01) cm^2 and (0.30 ± 0.01) cm^2.

2.2. Chemicals, Reagents and Solutions

The electrolytic solution (50 mL) was prepared based on a modification of Green's bath with Millipore Milli-Q water (MQ-water). The solution contained 174g/L $NiSO_4 \cdot 6H_2O$, 16 g/L $CuSO_4 \cdot 5H_2O$ (i.e., a [Ni(II)]/[Cu(II)] molar ratio of approximately 11), 87 g/L sodium citrate as a complexing agent, 0.2 g/L sodium dodecylsulfate as wetting agent and 0.5 g/L saccharine as refinement agent. The pH was fixed at 4.5 with addition of NaOH, and the working temperature was set at 303 K.

2.3. Electrode preparation

Before thin film deposition, substrates were degreased with acetone followed by isopropyl alcohol and MQ-water and, finally dipped in 1M H_2SO_4 to remove any oxides and organic residues. The electrolyte was de-aerated with argon gas before each experiment.

2.4. Procedure

An initial CV study was performed to establish the current densities suitable for the deposition of CuNi alloys with tuneable composition. A single cycle was run in each experiment, at a scan rate of 50 mV/s. The potential was swept from 0.25 V towards different cathodic limits, and then the scan was reversed towards the positive direction. Galvanostatic electrodeposition was run with applied current densities between -12 and -44 mA/cm^2 under mild stirring (200 rpm) using a magnetic stirrer bar. The galvanostatic mode with variable values of current density allowed the control of the alloy composition as well as the amount of charge (i.e., the thickness of the deposits). The thickness of CuNi layers was measured to be approximately 3 μm.

2.5. Characterization

Sample morphology and roughness of each sample were examined by scanning electron microscopy (SEM) using a Zeiss EVO® MA 10 microscope and a Zeiss MERLIN field emission scanning electron microscope (FE-SEM), and by atomic force microscopy (AFM) using a Dual Scope^{TM} C-26 system (Danish Micro Engineering) operating in AC mode. The AFM scanned surface area was 5 x 5 μm^2. The chemical composition of the samples was determined by energy dispersive X-ray spectroscopy (EDXS). The structure of the deposits was studied by X-ray diffraction (XRD). XRD patterns were recorded on a Philips X'Pert diffractometer using CuK_α radiation and θ-2θ configuration with 2θ in the range of 30 – 60º, 0.03º step size, and 10 s holding time. Cell parameter, crystallite sizes, microstrains and stacking fault probability were evaluated by fitting the XRD patterns using the Materials Analysis Using Diffraction (MAUD) Rietveld refinement program [15].

The mechanical properties of the films were evaluated by nanoindentation operating in the load control mode, using an UMIS device from Fischer-Cripps Laboratories equipped with a Berkovich pyramidal-shaped diamond tip. The maximum applied force was 10 mN and the thermal drift was kept below 0.05 nm/s. Following data acquisition of the load-displacement curves, proper corrections were applied for the initial penetration depth, tip blunting and instrument compliance. Hardness, H, and reduced Young's modulus, E_r, were then evaluated using the method of Oliver and Pharr [16]. The ratios H/E_r and H^3/E_r^2, related to the wear resistance and the resistance to plastic deformation, were also calculated. The elastic indentation energy, W_{el}, was determined as the area between the unloading indentation segment and the displacement axis, whereas the total indentation energy, W_{tot}, was estimated from the area underneath the loading indentation segment. The plastic energy, W_{pl}, was then evaluated as the difference ($W_{tot} – W_{el}$).

Corrosion tests were performed in a NaCl (3.5 wt%) solution at room temperature. A three-electrode cell configuration was used with a platinum sheet as CE and a Ag|AgCl RE containing1M NaCl as the outer solution. Once the sample was introduced into the solution, the open circuit potential, E_{OCP}, was typically achieved after 3 - 4 h of immersion. The system was considered stabilized when the potential fluctuations were smaller than 10 mV/h. Potentiodynamic polarization scans were performed from (E_{OCP} – 0.3) V to (E_{OCP} + 0.3) V with a scan rate of 0.1 mV/s, for an exposed area of 0.25 cm^2.

3. RESULTS AND DISCUSSION

3.1. CuNi thin film preparation

The CV curves recorded from the electrolytic solution are shown in Fig. 1a. One can observe that the Cu discharge starts at more positive potentials (around -0.10 V) than nickel deposition (around -0.85 V), as expected due to the nobler character of Cu. When the potential is sufficiently cathodic to permit the Ni discharge, the absolute value of the current density steeply increases, indicating that the incorporation of significant amounts of Ni into the deposits occurs rapidly within a relatively narrow potential range. In the anodic scan, different oxidation responses are observed depending on the applied cathodic limit. For the lowest cathodic limit, a single oxidation peak appears in the anodic sweep, probably related to the oxidation of previously deposited almost pure Cu. At larger cathodic limits a second oxidation peak, located at more positive potentials, develops. This feature is clearly related to the incorporation of Ni in the deposit formed during the cathodic sweep. The double-oxidation peak could indicate the formation of a two-phase deposit with dissimilar chemical composition. According to the results gleaned from the CV study, a suitable range of working current densities are chosen for the subsequent deposition of Cu-rich CuNi alloys.

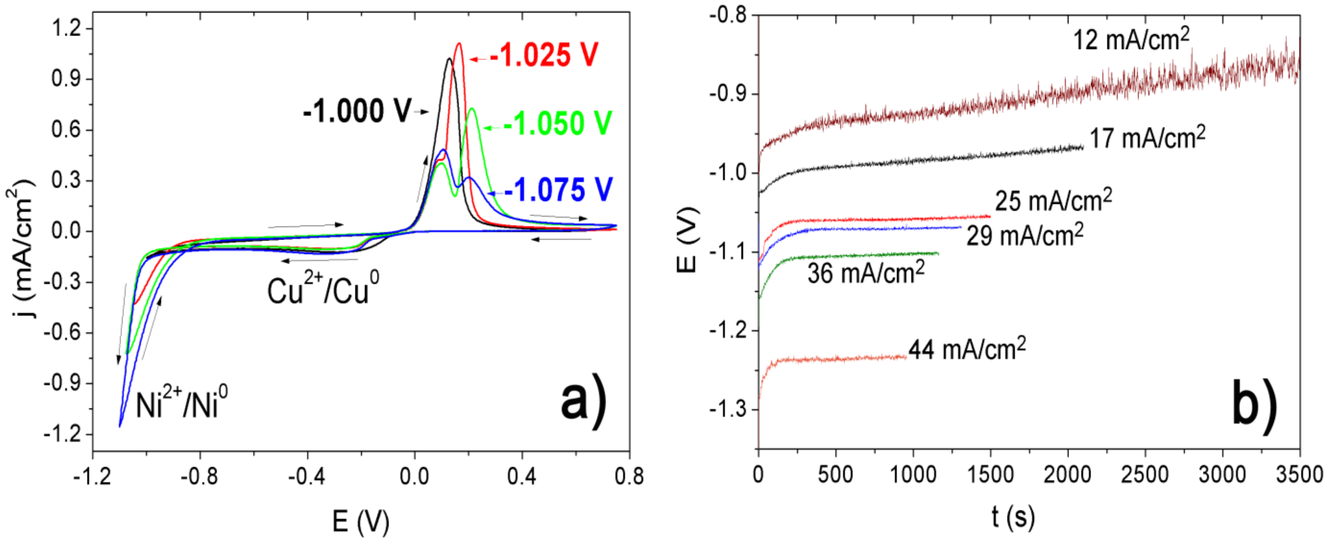

Figure 1. a) Cyclic voltammetry curves obtained at different cathodic limits between -1.000 and -1.075 V, at a scan rate of 50 mV/s. b) Galvanostatic curves for CuNi deposition at the indicated values of applied current densities.

Galvanostatic curves for CuNi deposition at current densities between -12 mA/cm^2 and -44 mA/cm^2 are shown in Fig. 1b. The selected current densities yield CuNi deposits with different composition. EDX analysis reveals that Cu content varied from 22 at% (at the lowest applied current density) to 97 at% (at the highest applied current density). Such a large variation can be ascribed to the different factors that limit the deposition of Cu and Ni. Namely, Cu discharge is diffusion-controlled, whereas the deposition of Ni is charge transfer-controlled. Therefore, deposits with higher Ni content are progressively obtained at higher overpotentials. Pure Cu deposits are not attained from this bath since little Ni (1-3 at%) enters the deposits despite using very low current densities.

3.2. Morphological and structural characterization

In our previous work [5,10,11] the effect of saccharine in reducing the surface roughness in Ni-rich Cu_xNi_{1-x} ($0.13 \leq x \leq 0.55$, atomic content) alloy films obtained from an electrolytic solution with a [Ni(II)]/[Cu(II)] molar ratio of 29 was investigated. However, we were unable to obtain flat and smooth Cu-rich samples from that bath formulation. A decrease of the [Ni(II)]/[Cu(II)] molar ratio to 11 has permitted the growth of flat deposits with higher Cu content, within the range $0.22 \leq x \leq 0.97$. SEM images (Fig. 2a-c) of the film surface indicate two different types of morphology depending on the Cu content. At very high Cu percentages (Fig. 2a) cauliflower-like deposits are obtained. For percentages below 70 at%, instead, the grain morphology cannot be resolved by conventional SEM imaging. An extremely fine-grained morphology was revealed using a FE-SEM microscope (Fig. 2c-inset). From the corresponding AFM images (Fig. 2d-f), the peak-to-valley (PTV) and root-mean-square (RMS) values were evaluated (Table 1).

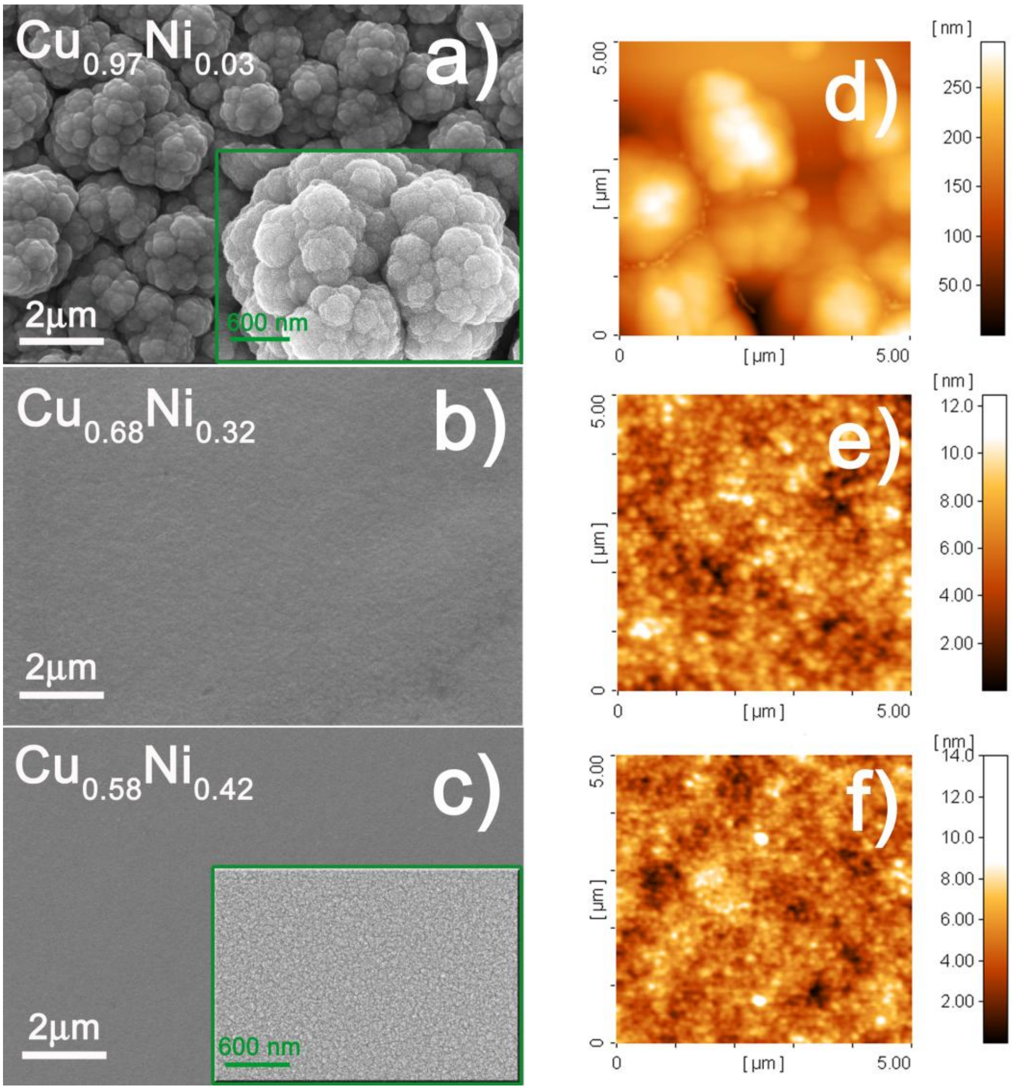

Figure 2. SEM (a-c) and corresponding AFM (d-f) images of CuNi alloys with different Ni content. Inset images in a) and c) show magnified details of sample surface obtained with a FE-SEM.

Table 1. Structural data obtained from XRD Rietveld refinement (lattice parameter a, crystallite size <D>, microstrains $<\varepsilon^2>^{1/2}$ and stacking fault probability α_{SF}) and AFM topological analysis (peak-to-valley value, PTV, and root-mean-square value, RMS).

Specimen composition	a (Å) [±10^{-4} Å]	<D> (nm)	$<\varepsilon^2>^{1/2}$ [±10^{-4}]	α_{SF} [±$5\cdot10^{-3}$]	PTV (nm)	RMS (nm)
$Cu_{0.97}Ni_{0.03}$	3.5836	90 ± 7	0.0010	0.015	309	52
$Cu_{0.68}Ni_{0.32}$	3.5690	39 ± 3	0.0017	0.010	13	2
$Cu_{0.46}Ni_{0.54}$	3.5602	44 ± 3	0.0018	0.013	28	2

The PTV and RMS are around 300 nm and 50 nm, respectively, for the sample with x = 0.97, while a sharp decrease of both parameters is observed for lower Cu contents. Hence, we can conclude that the new bath formulation permits the fabrication of very smooth thin films with Cu content $x \leq 70$ at%. It is well known that organic additives, such as saccharine, can change the microstructure of Cu/Ni multilayers avoiding the grain growth and favouring grain refinement [17]. Similarly, saccharine causes surface smoothing in CuNi alloys prepared from the Ni-rich bath formulation [5,10,11]. The saccharine concentration used in the present study still works fine for deposits with $x \leq 70$ at% Cu but is unable to induce the deposition of flat deposits for higher Cu contents. Actually, deposits featuring a Cu content between 70 and 90 at% are not easily obtained from this bath. Namely, while at low current densities Ni enters the deposits to a low extent (3 at% Cu for j = -12 mA/cm^2), a small increase in the applied current density gives rise to a large incorporation of Ni into the deposits (30 at% Cu for j = -22 mA/cm^2). This result is in agreement with the rather sharp increase in the current density values attributed to Ni discharge observed in the CV experiments (Fig. 1a).

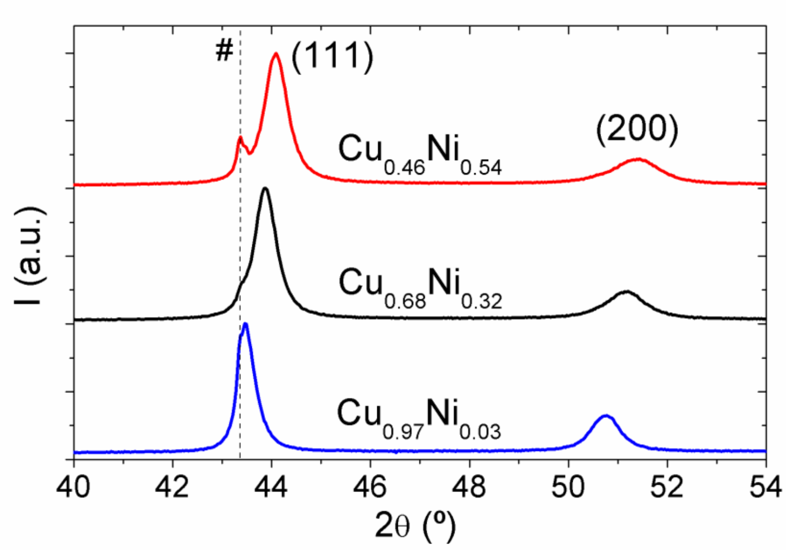

Figure 3. XRD patterns in the 40º – 54º 2θ region of CuNi samples with dissimilar copper content. The peak denoted by # belongs to the Cu seed layer.

Fig. 3 shows the XRD patterns of CuNi films with dissimilar Cu content (97, 68 and 46 at%). Notice that (111) and (200) fcc reflections shift towards higher angles as the Cu content is decreased, indicating an increase of the cell parameter, in agreement with the Vegard's law. Simultaneously, a peak located at the angular position corresponding to pure-Cu ($2\theta = 43.3^{\circ}$) is also observed. This reflection corresponds to the Cu seed layer, that for high Cu content becomes masked by the (111) fcc CuNi alloy reflection. Another important feature is the difference in width between the (111) and (200) peaks, which is indicative of the presence of stacking faults. The cell parameter, a, crystallite size, <D>, microstrains, $<\varepsilon^2>^{1/2}$, and stacking fault probability, α_{SF}, evaluated by Rietveld fitting are listed in Table 1. Crystallite size is kept below 100 nm for the complete range of compositions. Films with the highest Cu content (≥ 90 at%) show the largest crystallite sizes, while values at around 40 nm are observed in all the other films independent of Cu content. This difference in crystallite sizes is in agreement with the morphological differences observed among the different samples. As aforementioned, for very large Cu content effective nanostructuring is not achieved, and, therefore the crystallite size falls within the fine-grained regime.

The MAUD software used for the Rietveld refinement of the XRD patterns includes the Warren's formalism to evaluate the stacking fault (SF) probability, α_{SF} [18]. According to Warren's description of SF, $1/\alpha_{SF}$ designates the average number of planes between two consecutive SFs. The α_{SF} values in the Cu-rich CuNi films are of the order of 0.01 – 0.015 (Table 1) hence, on average one stacking fault should be present every each 60-100 atomic planes. Since the crystallite size of our samples is about 40 nm, this means that a large fraction of grains are likely to include one or even two intragranular stacking faults. In the Ni-rich films, values of α_{SF} around 0.007 and 0.008 were obtained [5], therefore lower than for the here-prepared Cu-rich CuNi films. The difference of α_{SF} with composition can be understood by realizing that the stacking fault energy (SFE) is higher for Ni than for Cu (i.e., it ranges between 124 and 250 mJ/m^2 for Ni [19, 20] and between 55 and 78 mJ/m^2 for Cu [20,21]). Therefore, an increase of Ni content in CuNi deposits probably increases the SFE and, consequently, would reduce the stacking fault probability as experimentally observed. However, even for similar CuNi compositions α_{SF} is higher for the samples prepared here than in the Ni-rich samples fabricated in [5]. For example $Cu_{0.55}Ni_{0.45}$ and $Cu_{0.44}Ni_{0.56}$ in [5], showed α_{SF} values around 0.008, while for the $Cu_{0.46}Ni_{0.54}$ sample herein investigated α_{SF} is 0.013. This discrepancy could stem from the different values of applied current densities used in both studies. Namely, near-stoichiometric samples in [5] were grown at a lower current density (-10 mA/cm^2) than the analogous samples fabricated in this work (-36 mA/cm^2). Higher current density implies faster deposition rates and could lead to higher density of intragranular nanotwins and other types of planar defects, as observed experimentally in electrodeposited Cu films [22].

3.3. Mechanical Properties

The mechanical properties of the films prepared in this work are plotted as a function of the Cu percentage in Fig. 4. For comparison, our previous results on Ni-rich CuNi films [5] are also included. Both the hardness, H, and the reduced Young's modulus, E_r, progressively decrease with an increase of the Cu content. The hardness varies from 7.9 GPa to 2.3 GPa and E_r from 198 GPa to 111 GPa as the Cu content increases from 12 to 97 at%. The values of hardness in Cu-richest CuNi alloys are in rather good agreement with those obtained, for example, in Cu-based alloys reinforced with Ni particles [23] or in fine-grained electroplated Cu films [24]. Remarkably, large hardness values are obtained for intermediate or low Cu percentages ($H \approx 7$ GPa), where the films exhibit a truly nanocrystalline microstructure. These films show comparable hardness values to those of electroplated nanocrystalline Ni-W alloys [25], nanocrystalline Ni-Co films [26] or nano-multilayered Cu-Ni films [27].

Several factors can influence the observed hardness variations. First, except for very low strain rates, plastic deformation in nanocrystalline Cu is generally dominated by dislocation propagation inside the crystals rather than grain boundary sliding [28]. Consequently, larger H values are expected as the crystallite size is reduced towards the sub-100 nm range, since in this case the amount of grain boundaries, which act as disruption sites for dislocation motion, becomes progressively higher (an effect often referred to as Hall-Petch) [29]. In this sense, the large number of stacking faults can also contribute to hardness because intragranular nanotwins hinder dislocation propagation in a similar way as high-angle grain boundaries [29,30].

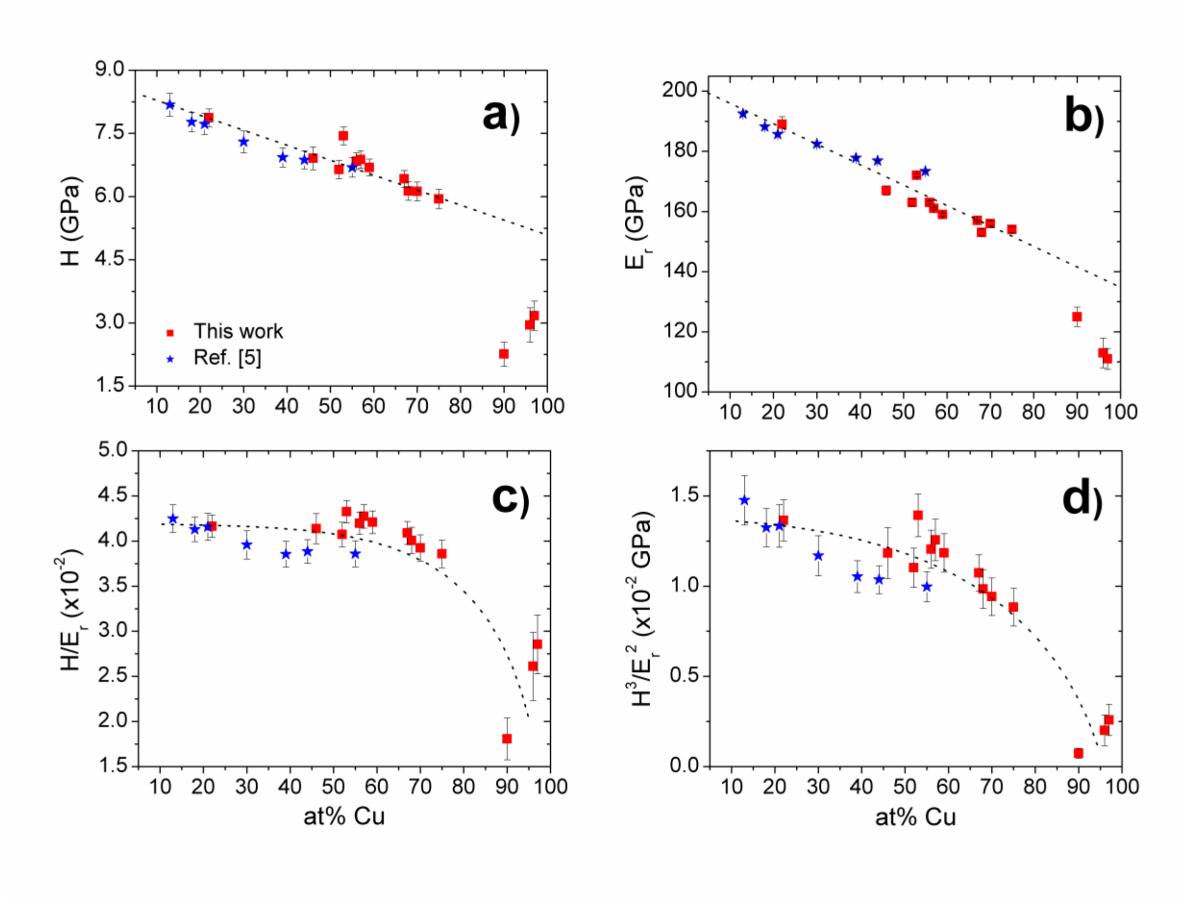

Figure 4. a) Hardness H, b) reduced Young's modulus E_r, c) wear resistance H/E_r, and d) resistance to plastic deformation H^3/E_r^2 for the samples analysed in this work, i.e., grown using a [Ni(II)]/[Cu(II)] molar ratio of 11 (red-square spots), and data obtained from our previous work [5] where the [Ni(II)]/[Cu(II)] molar ratio in the electrolyte was 29 (blue-star spots). The discontinuous lines in panels (a) and (b) are linear fits of the experimental data for Cu contents lower than 70 at%, whereas the discontinuous lines in panels (c) and (d) are guides to the eye.

Note that the decrease of H for Cu percentages larger than 90 at% can be attributed to the observed coarsening of the microstructure (Fig. 2). Besides grain size effects, it is well known that pure Ni exhibits higher yield stress, σ_y, than Cu [31]. Hence, since $H \approx 3\sigma_y$, the overall increase of H with the Ni percentage can be also ascribed to solution hardening [1,2].

Fig. 4b shows the variation of the reduced Young's modulus, E_r, on the Cu content. The reduced Young's modulus takes into account the elastic displacements that occur in both the specimen, with Young's modulus E and Poisson's ratio ν, and the diamond indenter, with elastic constants E_i and ν_i. The relationship between E_r and E can be expressed as [16]:

$$\frac{1}{E_r} = \frac{1-\nu^2}{E} + \frac{1-\nu_i^2}{E_i} \qquad \text{(Eq. 1)}$$

For diamond, E_i = 1140 GPa and ν_i = 0.07. Note that, because of the high Young's modulus of the tip and its low Poisson's ratio, E_r is typically very similar to E for most metallic materials (for CuNi films E is about 1-2 GPa higher than E_r). Since the Young's modulus of electrodeposited polycrystalline Ni (200 GPa [32]) is higher than of Cu (130 GPa [33]), a progressive decrease of E_r could be anticipated as the Cu content becomes progressively larger, as indicated with the discontinuous line in Fig. 4b. The good agreement between the expected values of E_r (dotted line) and the experimental data indicates that these samples do not exhibit appreciable porosity, particularly for Cu contents below 70 at%. Actually, it is well-known that even a low degree of porosity typically leads to a drastic reduction in E [34,35]. This can explain the pronounced decrease of E_r observed in Fig. 4b for Cu percentages higher than 70 at%. In a first approximation, the influence of porosity on the Young's modulus can be modelled using the approach of Ramakrishan and Arunachalam, which takes into account the intensification of pressure at the surface of spherical pores due to interactions between the pores and the surrounding bulk solid material [35]. For a given porosity fraction, P, the Young's modulus of the porous material, E_{porous}, is related to the Young's modulus of the fully dense material, E_{bulk}, according to [34,35]:

$$\frac{E_{porous}}{E_{bulk}} = \frac{(1-P)^2}{1+2P-3\nu P} \qquad \text{(Eq. 2)}$$

where ν is the Poisson's ratio of the bulk non-porous material (around 0.33 for CuNi in the investigated Cu-rich compositional range). Using Equations 1 and 2, the porosity level for Cu percentages lower than 70% is found to be essentially zero, whereas P attains values of around 7% and 11% for Cu contents of 90 and 97 at%, respectively.

From further analysis of the nanoindentation data one can estimate additional mechanical parameters such as the H/E_r, which is related to the wear resistance [36,37] (Fig. 4c), or the H^3/E_r^2 ratio, related to the resistance against plastic deformation [38]. In most of the investigated films H/E_r tends to a constant value of around 0.04, except for Cu content beyond 90 at%, where H/E_r is clearly lower, mainly because of the larger crystallite size. However, as shown in Fig. 4d, H^3/E_r^2 increases with the increase in the Ni content in a similar way as H. This is in agreement with the higher resistance against plastic deformation of Ni when compared to Cu, which typically shows better ductility.

From the analysis of the area of the load-unload nanoindentation curves, the total work of nanoindentation, W_{tot}, and the work recovered during unloading, W_{el}, can also be determined. The ratio W_{el}/W_{tot} provides an estimate of the elastic recovery of the films [39] and is an important parameter for impact loading applications. This ratio indicates how much energy is released from the material after being loaded and was found to decrease with the Cu percentage in the films. Although no direct correlation exists between the elastic recovery and hardness, finite element simulations of nanoindentation curves for a wide variety of elastic-plastic materials established the following relationship [40,41]:

$$\frac{W_{tot} - W_{el}}{W_{tot}} \cong 1 - 5\frac{H}{E_r} \qquad \text{(Eq. 3)}$$

As shown in Fig. 5, if $\frac{W_{tot} - W_{el}}{W_{tot}}$ is plotted against H/E_r a linear relationship is obtained and the slope fits rather well with the expected value, in agreement with other results in electroplated Co-Ni films [42].

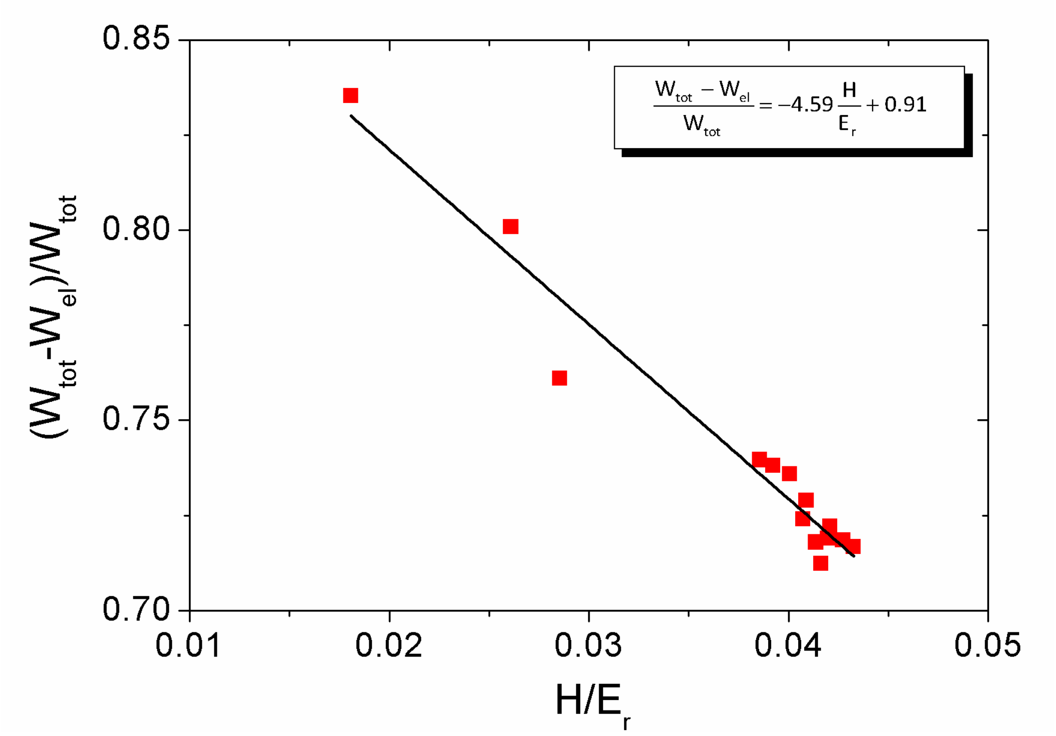

Figure 5. Dependence of the normalized plastic energy, $(W_{tot} - W_{el})/W_{tot}$, on the H/E_r ratio for the different investigated CuNi films. Note that the line is a linear fit of the experimental data.

Note that $W_{tot} - W_{el}$ refers to the plastic energy during nanoindentation, W_{pl}, and increases with the Cu content, indicating larger plasticity in the Cu-rich CuNi films than in the Ni-rich ones.

3.4. Corrosion behaviour

The corrosion behaviour of CuNi films has been assessed in aerated 3.5 wt% NaCl because this material is commonly used in applications involving seawater or chloride-containing media. Table 2 lists the E_{OCP} values of Cu_xNi_{1-x} (x = 0.97, 0.74, 0.58, 0.53, atomic content) samples and Cu/Ti/Si substrate (i.e., evaporated Cu seed layer).

Table 2. Open-circuit potential (E_{OCP}), corrosion potential (E_{corr}), corrosion current density (j_{corr}) and porosity values (P) estimated using Equation 4 corresponding to the substrate and the different CuNi alloys.

Specimen composition	E_{OCP} (V)	E_{corr} (V)	j_{corr} ($\mu A/cm^2$)	P (%)
Cu/Ti/Si (substrate)	-0.218	-0.195	15.9	--
$Cu_{0.97}Ni_{0.03}$	-0.171	-0.211	5.4	9.4
$Cu_{0.74}Ni_{0.26}$	-0.160	-0.156	1.8	1.5
$Cu_{0.58}Ni_{0.42}$	-0.169	-0.164	3.6	2.9
$Cu_{0.53}Ni_{0.47}$	-0.175	-0.171	3.0	4.0

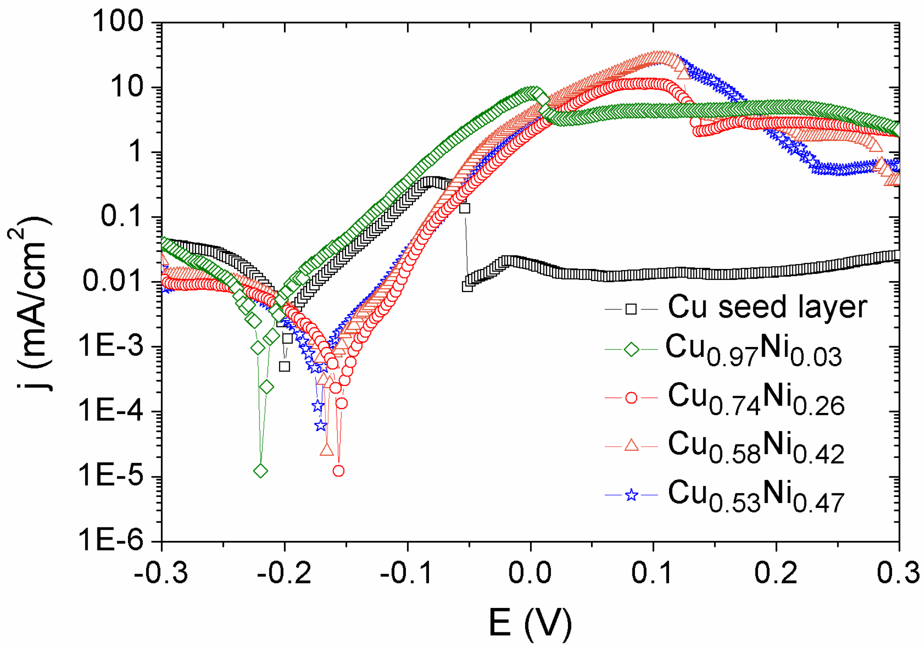

Figure 6. Representative potentiodynamic polarisation curves for various electrodeposited CuNi films and the bare substrate (i.e., evaporated Cu seed layer onto Ti/Si).

Compared to the substrate, the CuNi coatings show less negative E_{OCP} values except for x = 0.97. Indeed, for this sample, the E_{OCP} value is exceedingly different from the E_{corr}, probably indicating that complete stabilization was not achieved within the 3-4 hours of immersion. Representative potentiodynamic polarization curves are displayed in Fig. 6. While the cathodic branches do not indicate any special features, in the anodic branch the current density monotonically increases up to a maximum and then either a plateau is observed or a smooth current decrease is detected, indicating a possible passive region. The initial oxidative current would correspond to the formation of a passive oxide film that further protects the sample surface from ongoing corrosion. It has been claimed that the structure of these passive films actually consists of two layers, an outer CuO layer and an inner Cu_2O layer containing Ni^{2+} and Ni^{3+} [43]. Using Tafel extrapolation analysis, the E_{corr} and j_{corr} values have been determined (Table 2). It can be seen that the films with x = 0.74, 0.58 and 0.53 display similar parameters, all E_{corr} values being more positive and all j_{corr} values being lower compared to both the substrate (pure-Cu) and the $Cu_{0.97}Ni_{0.03}$ film. Rajasekaran and Mohan also observed an increase of the corrosion resistance in CuNi alloys electrodeposited on Cu substrate when compared to pure-Cu films deposited onto Cu substrate [44]. These results demonstrate that alloying Cu with significant amounts of Ni clearly improves the corrosion resistance of the material. This is in agreement with the well-known corrosion resistance of Constantan ($Cu_{55}Ni_{45}$) [2], a composition that has been used for many years as thermocouples. Actually, the films with x = 0.53 and 0.58 have a composition close to that of Constantan. Our values agree with those reported in the literature for CuNi coatings of similar composition and crystallite sizes. For example, E_{corr} values between -0.200 and -0.163 V vs. Ag|AgCl| 3M KCl were observed in $Cu_{0.55}Ni_{0.55}$ films with crystallize sizes ranging from 26 to 413 nm [10]. Interestingly, the films prepared in this work exhibit better anticorrosion properties in aerated NaCl medium than pulse-plated layers with higher Ni contents (70 at.%) but lower crystallite sizes (13 nm) [45]. It is important to stress that the rather good corrosion resistance of the here-prepared films can be partly attributed to their compactness (i.e., absence of porosity). The porosity (P) of a film can be estimated from the potentyodinamic polarization tests according to the following equation [46]:

$$P = \frac{R_{P,S}}{R_P} 10^{-(\Delta E_{corr}/\beta_a)} \qquad \text{(Eq. 4)}$$

where $R_{P,S}$ and R_P are the polarization resistances of the substrate and the deposited layer, respectively, ΔE_{corr} the potential difference between the bare substrate and the coated substrate, and β_a is the anodic Tafel coefficient of the substrate. The porosity values obtained from the linear potentiodynamic tests are in the range between 1.5% and 4.0% except for the film with the highest Cu content ($Cu_{0.97}Ni_{0.03}$) (Table 2). In this case, the porosity increases up to 9.4%, which is reasonable when accounting for the rough, cauliflower-like morphology shown by this electrodeposit (see Fig. 2a). Indeed, this sample shows the most negative E_{corr} value and the largest j_{corr} among the tested CuNi films. This could be partly ascribed to its intrinsic larger porosity, which would facilitate chlorine anion diffusion towards the film/substrate interface. Note that the obtained porosities fully agree with the values estimated from the Young's moduli (Eq. 2).

4. CONCLUSIONS

Nanocrystalline Cu-rich CuNi alloy films have been prepared by electrodeposition from an electrolytic bath containing Ni and Cu sulphates with a [Ni(II)]/[Cu(II)] molar ratio to 11. The decrease of the [Ni(II)]/[Cu(II)] molar concentration ratio from 29 (as in our previous Ni-rich CuNi films) to 11 extends the compositional range of the newly prepared films up to 97 at% Cu. These Cu-rich films follow similar structural, morphological and mechanical trends as our previous Ni-rich samples despite the well-known difficulties in controlling the growth of nanocrystalline smooth Cu-rich films. For CuNi deposits with a Cu content lower than 70 at%, SEM and XRD analyses reveal the occurrence of very flat surfaces accompanied by crystallite sizes of approximately 40 nm. The refined microstructure probably stems from the addition of saccharine in the electrolytic bath. The nanocrystalline character together with the high density of stacking faults, as evaluated from the XRD Rietveld refinements, are the main factors that contribute to the outstanding mechanical properties observed in these Cu-rich films. Actually, the mechanical properties (i.e., Young's modulus, hardness, wear resistance or resistance to plastic deformation) can be tailored by varying the deposit composition and are superior for intermediate or low Cu percentages. Concerning the corrosion performance in NaCl medium, the CuNi films display lower j_{corr} values and more positive E_{corr} values than the bare substrate, thus confirming the protective character of the here-prepared nanostructured, highly-dense CuNi alloys. For deposits with Cu content of 90-97 at% the crystallite size and the roughness are higher due to the occurrence of cauliflower-like surface morphologies and concomitant increase of porosity, ascribed to the lower effectiveness of saccharine in refining the grain size. This kind of morphology is also responsible for a decrease in strength and wear resistance and for poorer corrosion resistance, presumably due to the enhanced chloride anion diffusion towards the film/substrate interface.

ACKNOWLEDGEMENTS
This work has been partially financed by the 2009-SGR-1292 and MAT2011-27380-C02-01 research projects. M.D.B. was partially supported by an ICREA Academia award.

References

1. D.R. Askeland, P.P. Fulay and W.J.Wright, *The Science and Engineering of Materials*, Cengage Learning, Stamford (2011).
2. J.R. Davis, *Copper and Copper Alloys*, ASM International, United States of America (2001).
3. M. Metikoš-Huković, R. Babić, I. Škugor Rončević and Z. Grubač, *Desalination*, 276 (2011) 228-232.
4. V. Subramanian, P. Chandramohan, M.P. Srinivasan, S. Velmurugan and S.V. Narasimhan, *Corr. Sci.*, 49 (2007) 620-636.
5. E. Pellicer, A. Varea, S. Pané, B.J. Nelson, E. Menéndez, M. Estrader, S. Suriñach, M.D. Baró, J. Nogués and J. Sort, *Adv. Funct. Mater.*, 20 (2010) 983-991.
6. K. Lu, L. Lu and S. Suresh, *Science*, 324 (2009) 349-352.
7. M. Chen, E. Ma, K. J. Hemker, H. Sheng, Y. Wang and X. Cheng, *Science*, 23 (2003) 1275-1277.
8. L. Lu, M.L. Sui and K. Lu, *Science*, 25 (2000) 1463-1466.
9. M. Schlesinger and M. Paunovic, *Modern Electroplating*, John Wiley & Sons, New York (2000).
10. E. Pellicer, A. Varea, S. Pané, K.M. Sivaraman, B.J. Nelson, S. Suriñach, M.D. Baró, and J. Sort, *Surf. Coat. Technol.*, 205 (2011) 5285-5293.
11. E. Pellicer, A. Varea, K.M. Sivaraman, S. Pané, S. Suriñach, M.D. Baró, J. Nogués, B.J. Nelson and J. Sort, *ACS Appl. Mater. Interf.*, 3 (2011) 2265-2274.
12. E. Gómez, E. Pellicer and E. Vallés, *Electrochem. Commun.*, 6 (2004) 853-859.
13. Sh. Hassani, K. Raeissi and M.A. Golozar, *J. Appl. Electrochem.*, 38 (2008) 689-694.
14. S. Guan and B. J. Nelson, *J. Magn. Magn. Mater.*, 292 (2005) 49-58.
15. J. Sort, J. Nogués, S. Suriñach and M.D. Baró, *Philos. Mag.*, 83 (2003) 439-455.
16. W.C. Oliver and G.M. Pharr, *J. Mater. Res.*, 7 (1992) 1564-1583.

17. M. Troyon and L. Wang, *Appl. Surf. Sci.*, 103 (1996), 517-523.
18. B.E. Warren, *X-ray Diffraction*, Addison-Wesley, New York (1969).
19. R. Meyer and L.J. Lewis, *Phys. Rev. B*, 66 (2002) 052106.
20. F. Ebrahimi, A. Ahmed and H. Li, *Appl. Phys. Lett.*, 85 (2004) 3749-3751.
21. K. Youssef, M. Sakaliyska, H. Bahmanpour, R. Scattergood and C. Koch, *Acta Mater.*, 59 (2011) 5758-5764.
22. L. Lu, Y. Shen, X. Chen, L. Qian and K. Lu, *Science*, 304 (2004) 422-426.
23. D. Gu, Y. Shen and Z. Lu, *Mater. & Design*, 30 (2009) 2099-2107.
24. A. Ibáñez and E. Fatás, *Surf. Coat. Technol.*, 191 (2005) 7-16.
25. A.J. Detor and C. A. Schuh, *J. Mater. Res.*, 22 (2007) 3233-3248.
26. Y. Li, H. Jiang, W. Huang and H. Tian, *Appl. Surf. Sci.*, 254 (2008) 6865-6869.
27. Y. Kaneko, Y. Mizuta, Y. Nishijima and S. Hashimoto, *J. Mater. Sci.*, 40 (2005) 3231-3236.
28. H. Zhang, Z. Jiang and Y. Qiang, *Mater. Sci. Eng. A*, 517 (2009) 316-320.
29. M. Dao, L. Lu, R.J. Asaro, J.T.M. De Hosson and E. Ma, *Acta Mater.*, 55 (2007) 4041–4065.
30. X. Zhang, A. Misra, H. Wang, M. Nastasi, J. D. Embury, T. E. Mitchell, R. G. Hoagland and J. P. Hirth, *Appl. Phys. Lett.*, 84 (2004) 1096-1098.
31. G. V. Samsonov, *Handbook of the Physicochemical properties of the Elements*, IDI-Plenum, New York (1968).
32. T. Fritz, M. Griepentong, W. Mokwa and U. Schnakenberg, *Electrochim. Acta*, 48 (2003) 3029-3035.
33. T. H. Fang and W. J. Chang, *Microelectr. Engineer.*, 65 (2003) 231–238.
34. N. Chawla and X. Deng, *Mater. Sci. Eng. A*, 390 (2005) 98–112.
35. N. Ramakrishnan and V.S. Arunachalam, *J. Am. Ceram. Soc.*, 76 (1993) 2745-2752.
36. A.Leyland and A. Matthews, *Wear*, 246 (2000) 1-11.
37. C. Rebholz, A. Leyland, J.M. Schneider, A.A. Voevodin and A. Matthews, *Surf. Coat. Technol.*, 412 (1999) 120-121.
38. J. Musil, F. Kunc, H. Zeman and H. Poláková, *Surf. Coat. Technol.*, 154 (2002) 304-313.
39. A.C. Fisher-Cripps, *Nanoindentation*, Springer, New York (2004).
40. Y.-T. Cheng and C.-M. Cheng, *Appl. Phys. Lett.*, 73 (1998) 614-616.
41. W.C. Oliver and G.M. Pharr, *J. Mater. Res.*, 19 (2004) 3-20.
42. E. Pellicer, S. Pané, K.M. Sivaramen, O. Ergeneman, S. Suriñach, M.D. Baró, B.J. Nelson and J. Sort, *Mater. Chem. Phys.*, 130 (2011) 1380-1387.
43. M. Metikoš-Huković, I. Škugor, Z. Grubač and R. Babić, *Electrochim. Acta*, 55 (2010) 3123-3129.
44. N. Rajasekaran and S. Mohan, *J. Appl. Electrochem.*, 39 (2009) 1911-1916.
45. S.K. Ghosh, G.K. Dey, R.O. Dusane and A.K. Grover, *J. Alloy Comp.*, 426 (2006) 235-243.
46. J. Creus, H. Mazille and H. Idrissi, *Surf. Coat. Technol.*, 130 (2000) 224-232.